Rayleigh-based segmentation of ISAR images

S. HAMED JAVADI,[1,*] HICHEM SAHLI,[1,2] AND ANDRÉ BOURDOUX[1]

[1] *Interuniversity Micro-Electronics Center (IMEC), Kapeldreef 75, B-3001 Leuven, Belgium*
[2] *Informatics Dept., Vrije Universiteit Brussel (VUB), Pleinlaan 2, 1050 Brussels, Belgium*
[*] *hamed.javadi@imec.be*

Abstract: Inverse synthetic aperture radar (ISAR) provides a solution to increasing the radar angular resolution by observing a moving target over time. The high-resolution ISAR image should undergo a segmentation step to get the target's point cloud data which is then used for classification purposes. Existing segmentation algorithms seek an optimal threshold in an iterative manner which adds to the complexity of ISAR, resulting in a processing time increase. In this paper, we take advantage of the distribution of the ISAR image intensity, which is based on the Rayleigh distribution, and obtain an explicit relationship for the optimal segmentation threshold. The proposed segmentation algorithm alleviates the requirement for iterative optimization and its efficiency is shown using both simulated and experimental ISAR images.

1. Introduction

Inverse synthetic aperture radar (ISAR) is a well-established algorithm introduced by Walker [1] in 1980 for high-resolution radar imaging of a moving target using a stationary radar. It was quickly employed in plenty of applications, especially in military and aviation, for automatic target classification (ATC) and recognition (ATR) [2].

The range resolution of radars has improved with the large bandwidth provided by radar technologies such as frequency-modulated continuous wave (FMCW). On the other hand, the multi-input-multi-output (MIMO) technology has improved the angular resolution and alleviated the requirement for large-phased array antennas. Thanks to these advances in radars, the small-size MIMO mm-wave radars well fit in civilian applications such as autonomous vehicles and smart homes [3] where a great potential for ISAR is foreseen for object detection and identification [4–6].

While ISAR attempts to capture an image of targets by processing radar signals over time, the image is contaminated by different types of noises including speckle noise and sidelobes as well as smearing due to range and Doppler migration [7]. Therefore, before being fed to any classification/identification algorithm, ISAR images need to undergo a segmentation step in order for the target's point cloud to be extracted from the background noise. There exist several algorithms to filter out the speckle noise from the radar images [8, 9]; however, the segmentation approaches for ISAR images are limited to clustering the pixels (by, say, k-means) [10] and thresholding [11].

In this paper, we propose an efficient segmentation algorithm for ISAR images that not only filters out the speckle noise but also maintains the target's point cloud. Our work was motivated by the importance of noise reduction while keeping as many point clouds of the target as possible. The proposed segmentation algorithm belongs to the thresholding class of algorithms. However, it calculates the threshold based on the variance of the pixels, instead of estimating it by optimizing an objective function in an iterative manner, which is the case in Otsu and k-means. To this end, we first prove that the background noise follows a Rayleigh-based distribution. Then, any pixel outside of this distribution is considered to be coming from the target.

Accordingly, our proposed segmentation algorithm follows a similar approach of semi-supervised learning (SSL) [12]. SSL is proposed for anomaly detection in cases where only the data of the normal class is available and no (or only a small amount of) data of anomaly exists. Hence, supervised learning will not be possible. Instead, SSL estimates the boundary of the normal data out of which any data is detected as anomaly.

It is worth mentioning that the Rayleigh distribution has already been used in the segmentation literature for different types of images. The distribution is adopted in [13] for modeling the distribution of both the object and the background. Then, a threshold is calculated by minimizing the probability of miss-classification. In the end, a region-growing process is applied to further smooth the segmentation result. A similar approach is followed in [14] for the segmentation of echocardiographic images. In this paper, we explicitly show that the background noise follows a Rayleigh-based distribution and obtain a closed-form expression for the threshold.

The contributions of this paper can be summarized as follows:

- We prove that the background noise of ISAR images follows a Rayleigh-based distribution.
- Based on the Rayleigh-based distribution, we obtain an explicit relationship for calculating the optimal segmentation threshold. Since the threshold is located on the tail of the background distribution, it effectively filters out the speckle noise. Therefore, no extra speckle-filtering algorithm, such as the one proposed by Voci and Mascioli in [15], is needed.
- We present the complexity of our proposed segmentation algorithm and show that it is computationally much lighter than the common approaches.
- We conducted a practical ISAR imaging from a walking person using a MIMO radar. It is shown that a more informative point cloud of the target is obtained by the proposed segmentation algorithm compared to the Otsu and k-means algorithms.
- The effectiveness of the proposed algorithm is shown in both experimental and simulated scenarios.

The organization of this manuscript is as follows. In Sec. 2, the fundamentals of ISAR imaging as well as the Otsu algorithm is presented. Sec. 3 explains the proposed segmentation algorithm with its performance evaluated in Sec. 4. Finally, the paper is concluded in Sec. 5.

Notations

The notations used throughout the paper are listed in Table 1.

2. Background

2.1. ISAR

Radars basically transmit a sequence of waveforms during each coherent processing interval (CPI). Each waveform is referred to as a pulse or *chirp*. The received echo from the targets is demodulated by mixing with the original transmitted signal and gives the *beat signal* after filtering out the high frequencies.. The beat signal is collected in a matrix with each column representing the echo of the corresponding chirp (i.e., the echo of the first (second) chirp goes to the first (second) column, and so on). Accordingly, the matrix's row and column dimensions are referred to as the fast time and slow time, respectively. In MIMO radars, one matrix is collected per antenna. Therefore, a radar cube is generated at the end of each CPI. It is proved that an image of the observing target can be obtained by processing the radar data over time [16].

In radar imaging with ISAR [16], it is assumed that the radar is fixed and targets move. In ISAR, the movements of a target are categorized into radial and rotational motions (Fig. 1). Then, the basic idea is to compensate for the target's radial motion ($R(\mathbf{0})$ in Fig. 1) and reconstruct its image while it slightly rotates.

Table 1. The notations used in the paper.

Notation	description
$\alpha(.,.)$	2D ISAR image
c	Light speed
f	Frequency
$F_X(x)$	Distribution of X at x
r	Range
s	Scaling parameter
σ	Standard deviation
$s_B(.,.)$	Radar's beat signal
τ	Segmentation threshold
t_f	Fast time
t_s	Slow time
ω	Rotation rate

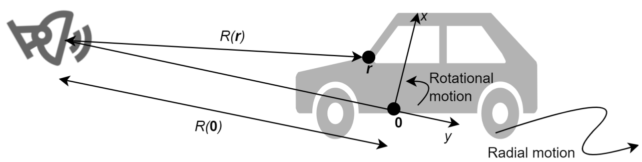

Fig. 1. The coordinate system in ISAR imaging.

It is proved that the image reconstruction can basically be accomplished by a 2D inverse Fourier transform (2D-IFT) of the compensated beat signal [17]:

$$\alpha\,(\eta,\nu) = \text{2D-IFT}\left[s_B(t_f,t_s)e^{j\frac{4\pi}{c}f_c\boldsymbol{R_0}(t_s)}\right]. \tag{1}$$

In the above equation, $s_B(t_f,t_s)$ is the beat signal in terms of fast time t_f and slow time t_s, f_c is the carrier frequency, and $\boldsymbol{R_0}\,(t_s)$ denotes the range of the coordinate origin which is assumed to change in slow time, i.e., its changes during fast time can be neglected. The target's image is also denoted by $\alpha\,(\eta,\nu)$ stating that the image is reconstructed in the domain of the round-trip time $\eta \triangleq \frac{2y}{c}$ and the Doppler frequency $\nu \triangleq \frac{2f_c}{c}\omega x$ wherein y and x are the range and cross-range, ω is the target's rotation rate, and c is the light speed.

Note that $\alpha\,(\eta,\nu)$ is complex-valued as the result of the IFT operator. The reconstructed image is the projection of the target's scatterers on a 2D plane which is in the radar line of sight (RLOS) direction (y axis in Fig. 2) and perpendicular to the effective rotation axis of the target.

Overall, ISAR includes two basic steps, as illustrated in Fig. 2. In the first step — referred to as *autofocus* —, the radial motion of the target is compensated. Then, the target's image is reconstructed by a 2D-IFT.

Any improvement in these steps will enhance the imaging quality. If the fast Fourier transform (FFT) is adopted, the major complexity of ISAR will be due to autofocus. The most common

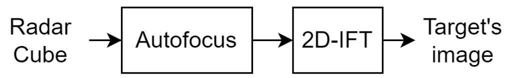

Fig. 2. Basic pipeline of ISAR imaging.

basic approaches to autofocus are the image-contrast-based autofocus (ICBA) [18, 19], image-Entropy-based autofocus [20], and the phase gradient algorithm (PGA) [21]. While the latter is non-parametric, the other two methods are parametric and provide more flexibility to manage the complexity. Although FFT provides a fast solution to image reconstruction, a more fitting method, especially when ICBA is used for autofocus, is the polynomial Fourier transform (PFT) [22, 23]. However, PFT is far more complex than FFT.

Apart from the two basic ISAR steps, further enhancement is achieved by time-windowing [24]. Time-windowing specifies the optimum set of the collected chirps that should be used for image reconstruction.

2.2. Otsu algorithm

Assume that the pixels of a gray-scale image are represented in L levels. Then, the Otsu algorithm seeks a threshold $k, 0 < k < L$ for dividing the pixels into two classes by optimizing the inter-class variance of the image. More specifically, the optimal threshold k^* is given by [11]:

$$k^* = \arg\max_k \frac{\left[\mu_T w(k) - \mu_k\right]^2}{w(k)\left[1 - w(k)\right]}, \tag{2}$$

where $w(k) \triangleq \sum_{i=1}^{k} p_i$, $\mu_k \triangleq \sum_{i=1}^{k} i p_i$, and $\mu_T \triangleq \sum_{i=1}^{L} i p_i$ with p_i denoting the ratio of the pixels at level i.

Being successful in the segmentation of gray-scale images, the Otsu algorithm became common, sometimes with slight modifications, in other applications [25, 26] including radar imaging [27, 28]. However, the variety in the pixels of a target is much higher in a radar image compared to a gray-scale image. This high variance results in miscalculating the inter-class variance in the Otsu algorithm, as will be shown in Sec. 4.

3. RaySe: Rayleigh-based segmentation

The idea here is to estimate the distribution of noise (background) in an ISAR image. Then, the segmentation threshold can be considered as the start of the higher tail of the distribution (Fig. 3).

A radar receives only thermal noise in the absence of any target. It is well-known that thermal noise has a flat power spectral density (PSD) which means that its (inverse) Fourier transform (FT) values are uniformly distributed among all frequency ranges. In other words, the pixels of an ISAR image (which is the 2D-IFT of the radar beat signals), in the absence of any target, are independent and identically distributed (i.i.d.) following a uniform distribution. On the other hand, a uniform distribution can be appropriately approximated by a Gaussian distribution. This approximation is especially more accurate in MIMO radars where each pixel, after beamforming, becomes the sum of several uniformly-distributed random variables (RVs) [17]. Therefore, the distribution of pixel (r, f) of an ISAR image is approximately given by:

$$\alpha(r, f) \sim \mathcal{CN}\left(0, \sigma^2\right), \tag{3}$$

where $\mathcal{CN}\left(0, \sigma^2\right)$ denotes a complex normal distribution with mean 0 and variance σ^2. Defining the real and imaginary parts of the pixel as $\alpha_r \triangleq \mathrm{Re}\left[\alpha(r, f)\right]$ and $\alpha_i \triangleq \mathrm{Im}\left[\alpha(r, f)\right]$, respectively, gives:

$$\alpha_r, \alpha_i \sim \mathcal{N}\left(0, \sigma^2\right), \tag{4}$$

with $\mathcal{N}(0, \sigma^2)$ being a normal distribution with mean 0 and variance σ^2.

For segmentation, it is common to use the power of an image in dB. The power of the pixel is given by $w \triangleq 10 \log (I(\alpha_r, \alpha_i))$ with $I(\alpha_r, \alpha_i) \triangleq \sqrt{\alpha_r^2 + \alpha_i^2}$ following a Rayleigh distribution with scale parameter σ [29]. It is straightforward to prove that the cumulative density function (CDF) of w is given by:

$$F_W(w) = P(W < w) = F_I\left(10^{\frac{w}{10}}\right), \tag{5}$$

where $F_I(.)$ denotes the CDF of the Rayleigh distribution.

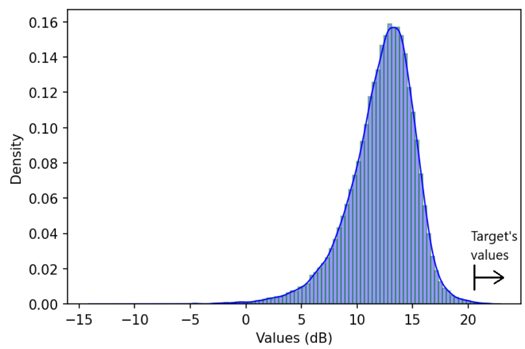

Fig. 3. The distribution of an ISAR image power.

If a target appears in the radar FoV, its values will lie in the higher tail of the background distribution, as seen in Fig. 3. For segmentation, it suffices to set the threshold as the starting point of the tail. Accordingly, the Rayleigh-based segmentation (RaySe) algorithm is presented in Fig. 4 wherein s is a scaling parameter of the threshold with a default value of 1. It can be used to adjust the threshold τ depending on the signal-to-noise ratio (SNR) of the ISAR images. In fact, there is a compromise between getting more pixels as the target's point cloud and filtering the noise (and sidelobes). The former can be achieved by $s < 1$ at the cost of having more falsely detected image pixels. The latter is appropriate for higher SNRs. There, the target scatterers give sufficiently high image values; so, they can effectively be separated from noise with a larger segmentation threshold by setting $s > 1$.

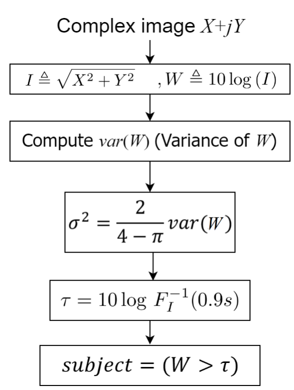

Fig. 4. The Rayleigh-based segmentation (RaySe) pipeline. s is a scaling parameter with a default of value 1.

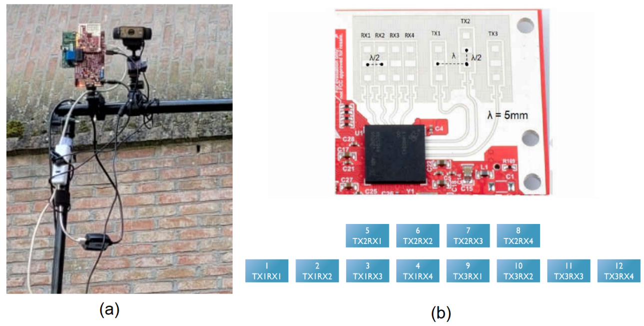

Fig. 5. (a) The setup used for data recording includes a radar and a normal webcam. (b) The radar's antenna layout and its virtual array (copied from [31]).

Complexity of RaySe

The RaySe algorithm is based on the computation of the variance of the image power. Accordingly, its complexity is $O(N_I)$ where N_I denotes the number of the image's pixels. Therefore, Rayse is less complex than the common Otsu algorithm with the complexity of $O(LN_I)$ wherein L indicates the number of the levels of the image power. Note that L is normally large since there is a huge difference between the strongest and weakest pixels of an ISAR image. The RaySe complexity is also lower than k-means whose complexity is $O\left(N_I^2\right)$ [30].

4. Evaluation results

We evaluate the performance of RaySe in both experimental and simulated scenarios and compare it against the Otsu and k-means algorithms as the most common segmentation methods. The k-means algorithm was run with $k = 3$ in 300 iterations. Then, the cluster with the highest centroid is considered the point cloud of the target. Although only two clusters (namely, the target and the background) are needed, using $k = 3$ gives a better segmentation result since the ISAR image values are categorized by k-means into "smaller than the lower tail", "background noise", and "larger than the higher tail" (Fig. 3).

4.1. Experimental evaluation

The IWR6843ISK radar of Texas Instruments was used for ISAR imaging from a moving person. This radar has three transmitters and four receivers. It was installed together with a webcam (HD Pro of LogiTech) on a tripod at a height of around $3m$ from the ground and a tilt of around 13^o toward the ground. The setup and the radar antenna layout are shown in Fig. 5.

The radar worked with the setting of Table 2 that provides the following specifications:

- Range resolution $\rho_r = 4.61cm$;
- Maximum unambiguous range $R_{max} = 11.79m$;
- Velocity resolution $\rho_v = 0.027m/s$;
- Maximum unambiguous velocity $V_{max} = 11.04m/s$.

As seen in Fig. 5-b, the virtual antenna array consists of two rows indicating poor elevation resolution. Hence, we reconstruct one ISAR image per row and then sum up the two images after phase compensation. To this end, beamforming is carried out with the center of each row as a reference.

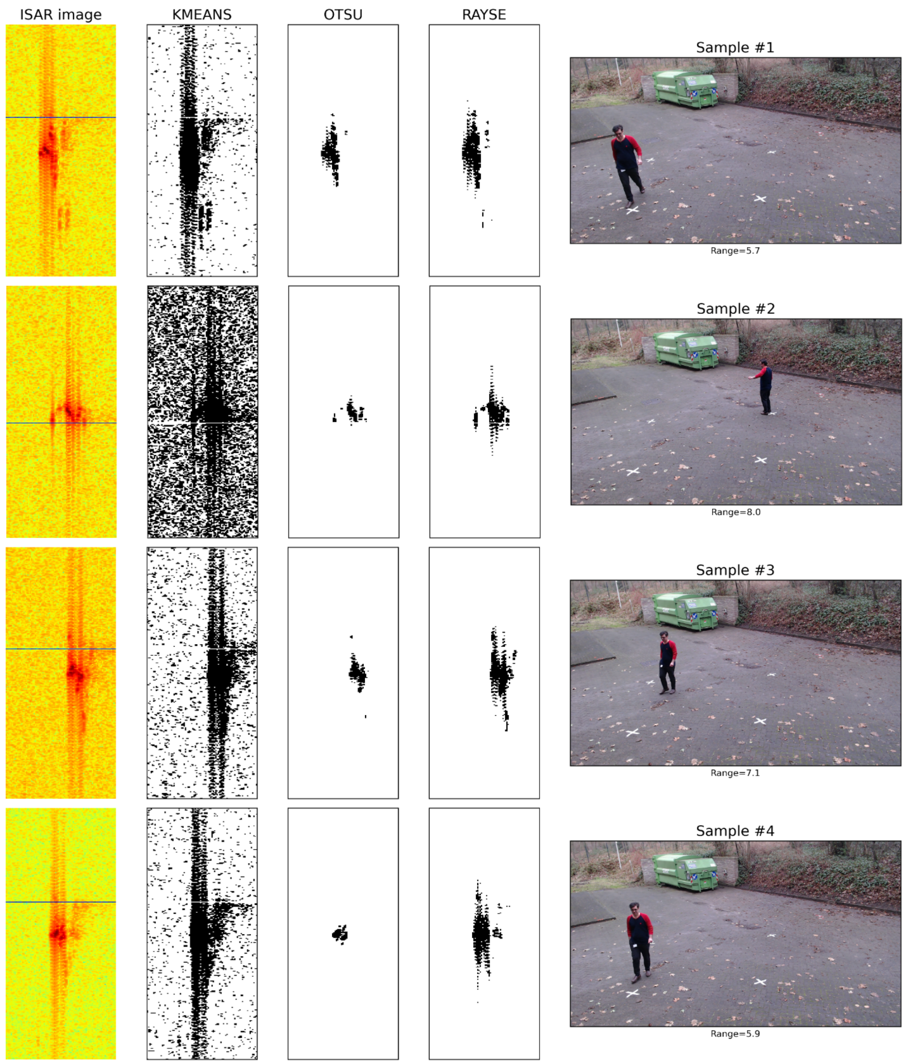

Fig. 6. Comparison of RaySe against Otsu and k-means in practical ISAR imaging from a person.

Table 2. The setting of the radar used for experimental evaluation.

Radar parameter	Value
Start frequency (GHz)	60.1221
Bandwidth (GHz)	3.257
Pulse repetition time (μs)	36.66
Coherent processing time (ms)	90
Number of chirps per frame	255
Number of samples per chirp	256
Sampling frequency (MHz)	9.6

Fig. 6 shows the segmentation results of ISAR imaging from a walking person. In Fig. 6, the power of the ISAR images in dB is illustrated while the segmentation results are thresholded. For RaySe, we used scale parameter $s = 1.05$ to better filter the noise.

As seen in Fig. 6, k-means has failed to properly do the segmentation. The reason is that k-means is intrinsically appropriate for symmetric data (Because k-means classifies the points based on estimating the centroids of each cluster) [32] which is not the case with the ISAR images (and any other sorts of data based on radar signal). Furthermore, our results suggest that k-means should be used together with a smoothing filter, similar to what is proposed in [15], in order to have the speckle noise of the ISAR image removed.

Otsu successfully filters the speckle noise but also plenty of the informative point cloud of the ISAR image. As explained in Sec. 2.2, the Otsu algorithm maximizes the inter-class variance. In ISAR images, as seen in Fig. 6, there are often several pixels with extremely high values that make the Otsu algorithm give a higher segmentation threshold.

In our framework, ISAR imaging is used for a better reconstruction of the pedestrian shape. Hence, we expect the segmentation to produce a better shape of the target. We visually inspected the segmentation results obtained using the Otsu algorithm and the proposed RaySe approach. As can be seen in Fig.6 several parts of the foreground are misclassified by the Otsu algorithm (the leg in sample #1, and the head and legs in sample #4). This is also confirmed in Fig. 6, in which the segmentation obtained using RaySe produces a more informative point could of the human body.

The histograms of the ISAR images of the examined samples are shown in Fig. 7 with the thresholds of the segmentation algorithms listed in Table 3. As shown, RaySe gives the most appropriate threshold that filters out the speckle noise while keeping the informative point clouds.

Table 3. The segmentation thresholds for the samples of Fig. 6.

Sample no.	#1	#2	#3	#4
k-means	43.87	40.13	42.93	43.32
Otsu	53.30	53.98	54.96	59.21
RaySe	48.82	47.28	48.37	48.19

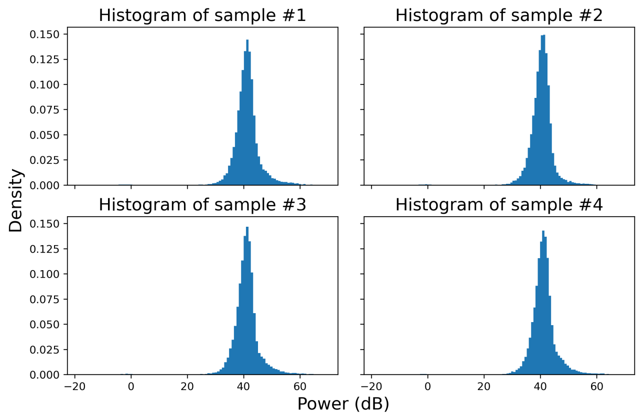

Fig. 7. The histogram of the ISAR images of the samples shown in Fig 6.

4.2. Simulation evaluation

For evaluation of the RaySe performance on simulated data, the dataset provided by [33] was used. This dataset provides ISAR images of moving automotive targets in different scenarios. Using three samples from this dataset, the segmentation results are shown in Fig. 8. As seen, k-means has given better results than before since the simulated data includes less speckle noise and weaker sidelobes. However, fewer scatterers of the target are given by Otsu. Compared to Otsu and k-means, RaySe has provided a more informative point cloud of the target.

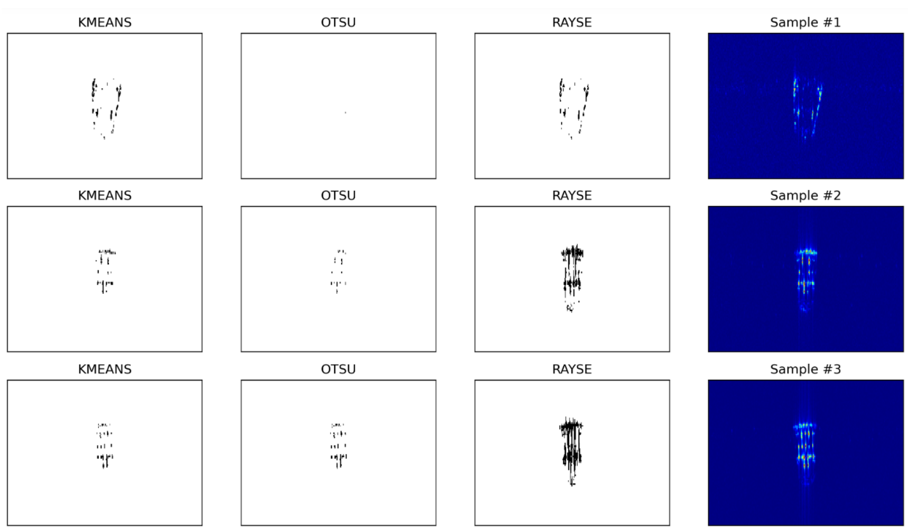

Fig. 8. Comparison of RaySe against Otsu and k-means in simulated ISAR imaging from a car.

5. Conclusions and future directions

In this paper, we proposed the Rayleigh-based segmentation (RaySe) algorithm as an efficient and computationally light method of extracting the target's image out of the background in ISAR images. Inspired by the concept of semi-supervised learning, the RaySe algorithm was developed by obtaining the distribution of the background noise. Then, any pixel with a value exceeding the higher tail of the distribution is considered as belonging to the target. The significance of the proposed algorithm is that it effectively filters out the speckle noise and meanwhile keeps the informative point clouds of the target which are essential for classification and any other machine-learning-based algorithms. The effectiveness of RaySe compared to the commonly used approaches, namely Otsu and k-means, was shown through experimental and simulated scenarios.

The proposed segmentation algorithm incorporates a parameter for more calibration of the segmentation threshold. Including a self-calibration method where this parameter is adjusted by optimizing an appropriate objective function (such as the image contrast or entropy) can be considered as a future algorithm development. Furthermore, the proposed RaySe algorithm targets the binary classification of ISAR images. Extending RaySe to address multi-class segmentation is an interesting topic for future work that may well fit in synthetic aperture radar (SAR) images where an environment including different objects needs to be segmented.

Funding. The research leading to these results has received funding from IMEC.ICON and Flanders Innovation & Entrepreneurship (nr HBC.2020.3106) – Project Surv-AI-llance.

Disclosures. The authors declare no conflicts of interest.

Data Availability. Data underlying the results presented in this paper are not publicly available at this time but may be obtained from the authors upon reasonable request. Also, the authors partly used the dataset available in Ref. [33].

References

1. J. L. Walker, "Range-doppler imaging of rotating objects," IEEE Trans. on Aerosp. Electron. Syst. **AES-16**, 23–52 (1980).
2. S. Musman, D. Kerr, and C. Bachmann, "Automatic recognition of isar ship images," IEEE Trans. on Aerosp. Electron. Syst. **32**, 1392–1404 (1996).
3. S. H. Javadi and A. Farina, "Radar networks: A review of features and challenges," Inf. Fusion **61**, 48–55 (2020).
4. S. S. Ram, "Fusion of inverse synthetic aperture radar and camera images for automotive target tracking," IEEE J. Sel. Top. Signal Process. pp. 1–14 (2022).
5. C. J. Li and H. Ling, "Wide-Angle, Ultra-Wideband ISAR Imaging of Vehicles and Drones," Sensors **18** (2018).
6. Z. Peng, J. M. Muñoz-Ferreras, Y. Tang, C. Liu, R. Gómez-García, L. Ran, and C. Li, "A Portable FMCW Interferometry Radar With Programmable Low-IF Architecture for Localization, ISAR Imaging, and Vital Sign Tracking," IEEE Trans. on Microw. Theory Tech. **65**, 1334–1344 (2017).
7. A. Bourdoux and M. Bauduin, "Near-optimal Range Migration and Doppler Ambiguity Compensation for FMCW Radars," in *2022 IEEE Radar Conference (RadarConf22),* (2022), pp. 1–6.
8. Z. Anjun, X. Yang, L. Jia, J. Ai, and J. Xia, "SRAD-CNN for adaptive synthetic aperture radar image classification," Int. J. Remote. Sens. **40**, 3461–3485 (2019).
9. N. Tabassum, A. Vaccari, and S. Acton, "Speckle removal and change preservation by distance-driven anisotropic diffusion of synthetic aperture radar temporal stacks," Digit. Signal Process. **74**, 43–55 (2018).
10. D. Xiao, F. Su, and J. Wu, "Multi-target ISAR imaging based on image segmentation and Short-time Fourier Transform," in *2012 5th International Congress on Image and Signal Processing,* (2012), pp. 1832–1836.
11. N. Otsu, "A threshold selection method from gray-level histograms," IEEE Trans. on Syst. Man, Cybern. **9**, 62–66 (1979).
12. O. Chapelle, B. Schölkopf, and A. Zien, *Semi-Supervised Learning*, vol. 2 (MIT press, Cambridge, MA, USA, 2006).
13. X. Chen, D. Bless, and Y. Yan, "A Segmentation Scheme Based on Rayleigh Distribution Model for Extracting Glottal Waveform from High-speed Laryngeal Images," in *2005 IEEE Engineering in Medicine and Biology 27th Annual Conference,* (2005), pp. 6269–6272.
14. A. Belaid and D. Boukerroui, "Local maximum likelihood segmentation of echocardiographic images with Rayleigh distribution," Signal, Image Video Process. **12**, 1087–1096 (2018).
15. F. Voci and F. Mascioli, "ISAR image segmentation by non linear diffusion equation," in *2006 IEEE Conference on Radar,* (2006), pp. 4 pp.–.
16. D. A. Ausherman, A. Kozma, J. L. Walker, H. M. Jones, and E. C. Poggio, "Developments in radar imaging," IEEE Trans. on Aerosp. Electron. Syst. **AES-20**, 363–400 (1984).

17. V. C. Chen and M. Martorella, *Inverse Synthetic Aperture Radar Imaging - Principles, Algorithms and Applications* (Scitech publishing, Edison, NJ, USA, 2014).
18. F. Berizzi and G. Corsini, “Autofocusing of inverse synthetic aperture radar images using contrast optimization,” IEEE Trans. on Aerosp. Electron. Syst. **32**, 1185–1191 (1996).
19. M. Martorella, F. Berizzi, and B. Haywood, “Contrast maximisation based technique for 2-D ISAR autofocusing,” IEE Proc. - Radar, Sonar Navig. **152**, 253–262(9) (2005).
20. L. Xi, L. Guosui, and J. Ni, “Autofocusing of ISAR images based on entropy minimization,” IEEE Trans. on Aerosp. Electron. Syst. **35**, 1240–1252 (1999).
21. D. Wahl, P. Eichel, D. Ghiglia, and C. Jakowatz, “Phase gradient autofocus-a robust tool for high resolution SAR phase correction,” IEEE Trans. on Aerosp. Electron. Syst. **30**, 827–835 (1994).
22. I. Djurović, T. Thayaparan, and L. Stanković, “Adaptive Local Polynomial Fourier Transform in ISAR,” EURASIP J. on Adv. Signal Process. **2006**, 1687–6180 (2006).
23. M. Martorella, “Novel approach for isar image cross-range scaling,” IEEE Trans. on Aerosp. Electron. Syst. **44**, 281–294 (2008).
24. M. Martorella, “Chapter 19 - Introduction to Inverse Synthetic Aperture Radar,” in *Academic Press Library in Signal Processing: Volume 2,* vol. 2 of *Academic Press Library in Signal Processing* N. D. Sidiropoulos, F. Gini, R. Chellappa, and S. Theodoridis, eds. (Elsevier, 2014), pp. 987–1042.
25. X. Yuan, J. Martínez, M. Eckert, and L. López-Santidrián, “An Improved Otsu Threshold Segmentation Method for Underwater Simultaneous Localization and Mapping-Based Navigation,” Sensors **16**, 1148 (2016).
26. Y. Zhan and G. Zhang, “An Improved OTSU Algorithm Using Histogram Accumulation Moment for Ore Segmentation,” Symmetry **11** (2019).
27. A. Manno-Kovacs, E. Giusti, F. Berizzi, and L. Kovács, “Image Based Robust Target Classification for Passive ISAR,” IEEE Sensors J. **19**, 268–276 (2019).
28. H. Yang, Y. Zhang, and W. Ding, “A Fast Recognition Method for Space Targets in ISAR Images Based on Local and Global Structural Fusion Features with Lower Dimensions,” Int. J. Aerosp. Eng. **2020**, 1687–5966 (2020).
29. H. C. Papadopoulos, G. W. Wornell, and A. V. Oppenheim, “Sequential signal encoding from noisy measurements using quantizers with dynamic bias control,” IEEE Trans. Inf. Theory **47**, 978–1002 (2001).
30. M. K. Pakhira, “A linear time-complexity k-means algorithm using cluster shifting,” in *2014 International Conference on Computational Intelligence and Communication Networks,* (2014), pp. 1047–1051.
31. “User’s Guide - 60GHz mmWave Sensor EVMs,” Tech. rep., Texas Instruments (2018).
32. D. Olszewski, “k-means clustering of asymmetric data,” in *Hybrid Artificial Intelligent Systems,* E. Corchado, V. Snášel, A. Abraham, M. Woźniak, M. Graña, and S.-B. Cho, eds. (Springer Berlin Heidelberg, Berlin, Heidelberg, 2012), pp. 243–254.
33. N. Pandey and S. Sundar Ram, *Dataset of simulated inverse synthetic aperture radar (ISAR) images of automotive targets.* (IEEE Dataport, 2021).